Electrochimica Acta 332 (2020) 135267

Contents lists available at ScienceDirect

Electrochimica Acta

journal homepage: www.elsevier.com/locate/electacta

Nanoscale electrochemical visualization of grain-dependent anodic iron dissolution from low carbon steel

L.C. Yule [a, b], V. Shkirskiy [a], J. Aarons [c], G. West [b], B.A. Shollock [b, d, **], C.L. Bentley [a, ***], P.R. Unwin [a, *]

[a] Department of Chemistry, University of Warwick, Coventry, CV4 7AL, UK
[b] Warwick Manufacturing Group, University of Warwick, Coventry, CV4 7AL, UK
[c] Department of Physics University of Warwick, Coventry, CV4 7AL, UK
[d] Kings College London, Strand, London, WC2R 2LS, UK

ARTICLE INFO

Article history:
Received 2 September 2019
Received in revised form
31 October 2019
Accepted 10 November 2019
Available online 13 November 2019

Keywords:
Corrosion science
Scanning electrochemical cell microscopy
Nanoelectrochemistry
Metal dissolution
Scanning probe microscopy

ABSTRACT

The properties of steels and other alloys are often tailored to suit specific applications through the manipulation of microstructure (*e.g.*, grain structure). Such microscopic heterogeneities are also known to modulate corrosion susceptibility/resistance, but the exact dependency remains unclear, largely due to the challenge of probing and correlating local electrochemistry and structure at complex (alloy) surfaces. Herein, high-resolution scanning electrochemical cell microscopy (SECCM) is employed to perform spatially-resolved potentiodynamic polarisation measurements, which, when correlated to co-located structural information from electron backscatter diffraction (EBSD), analytical scanning electron microscopy (SEM) and scanning transmission electron microscopy (STEM), reveal the relationship between anodic metal (iron) dissolution and the crystallographic orientation of low carbon steel in aqueous sulfuric acid (pH 2.3). Considering hundreds of individual measurements made on each of the low-index planes of body-centred cubic (bcc) low carbon steel, the rate of iron dissolution, and thus overall corrosion susceptibility, increases in the order (101) < (111) < (100). These results are rationalized by complementary density functional theory (DFT) calculations, where the experimental rate of iron dissolution correlates with the energy required to remove (and ionise) one iron atom at the surface of a lattice, calculated for each low-index orientation. Overall, this study further demonstrates how nanometre-resolved electrochemical techniques such as SECCM can be effectively utilised to vastly improve the understanding of structure–function in corrosion science, particularly when combined with complementary, co-located structural characterisation (EBSD, STEM *etc.*) and computational analysis (DFT).

1. Introduction

The microstructural features of steel and other alloys, such as grains of different crystal orientation, grain boundaries and (sub) microscale inclusions, play an important role in the formation of the local anodic and cathodic cells that drive corrosion processes [1]. Indeed, many studies have attempted to resolve the relationship between surface structure and electrochemical activity with metals such as iron [2–5], 316 L stainless steel [6] and aluminium [7]. Although such studies report that the crystal orientation does influence corrosion behaviour, a consistent trend or explanation for this behaviour has not been forthcoming. This is largely attributed to the difficulty in probing local electrochemistry and structure in the same area at complex surfaces, meaning that in practice measurements are often limited to a few measurements on single grains [8]. For this reason, there is a need for techniques that can probe corrosion-related phenomena with high spatial-resolution, an application where scanning electrochemical probe microscopy (SEPM) techniques are most powerful [9].

Presently, the most widely-used SEPM method in corrosion

* Corresponding author. Department of Chemistry, University of Warwick, Coventry, CV4 7AL, UK.
** Corresponding author. Kings College London, Strand, London, WC2R 2LS, UK.
*** Corresponding author. Department of Chemistry, University of Warwick, Coventry, CV4 7AL, UK.
E-mail addresses: barbara.shollock@kcl.ac.uk (B.A. Shollock), c.bentley.1@warwick.ac.uk (C.L. Bentley), p.r.unwin@warwick.ac.uk (P.R. Unwin).

https://doi.org/10.1016/j.electacta.2019.135267

science is scanning electrochemical microscopy (SECM) [10,11]. Although microscale measurements can be made readily with SECM, it is important to note that SECM interrogates electrochemical processes *indirectly* by measuring fluxes and concentrations at an ultramicroelectrode probe. The application of SECM in corrosion-related measurements is non-trivial, particularly at the nanoscale, for several reasons including topographical changes in the surface and complex intermediate/product speciation (*e.g.*, metal ions in anodic dissolution), which need to be easily detected at the tip. Applying an alternating current in an SECM configuration (AC-SECM) partially resolves these issues, since no redox mediator is required [12,13]. Nevertheless, the quantitative interpretation of data is complicated due to the convolution in the AC-SECM signal of both topography (tip-substrate distance) and electrode kinetics of corroding interfaces.

In contrast, the electrochemical droplet cell (EDC) technique [14,15] probes electrochemistry *locally* and *directly* by contacting a small (micrometric) area of the surface of interest under a droplet formed at the end of a fluidic probe. Data analysis in the EDC format is straightforward, as well-known electrochemical techniques (*e.g.,* potentiodynamic polarisation) are applied. Two major downsides of the conventional EDC technique are its limited spatial-resolution and low throughput [16]. The EDC has been used to study the degradation of a number of materials, including 304 stainless steel [15,17] and aluminium [7,18,19]. A few works have reported the application of the EDC technique to the dissolution of polycrystalline Fe in $NaNO_3$ [3] and acetate buffer [2]. The measurements were limited to a few points of *ca.* 100 μm size on single (100), (101) and (111) crystallographic planes. In these studies, the dissolution rate increased in the sequence (100) < (101) < (111).

Scanning electrochemical cell microscopy (SECCM) is the next generation of the EDC technique, making considerable improvements in terms of spatial-resolution, speed and usability [20,21]. In essence, through the use of much finer pipets (typically 30 nm to 1 μm in diameter [22]) and piezoelectric positioners, SECCM automates the EDC technique, making possible the rapid translation of a nanoscale droplet cell across an electrode surface to perform high-resolution electrochemical mapping. SECCM has been shown to be extremely powerful for nanoscale structure–function studies, being used to probe the electrochemical activity of, for example, molybdenum disulfide [23], sp^2 carbon materials [24], polycrystalline metals [25–27], iron nickel sulfide catalysts [28], metallic nanoparticles [29,30], semiconductors [31] and battery materials [32]. SECCM is also a potentially powerful tool for corrosion-related research, as demonstrated by our recent proof-of-concept studies investigating the role of microstructure on the passivating behaviour of low carbon steel in pH neutral solutions of KNO_3 [33].

In this study, the local rate of iron dissolution has been correlated to the crystal orientation in order to unveil how different grains may support anodic processes in the formation of galvanic corrosion cells. With SECCM, thousands of spatially-resolved electrochemical (potentiodynamic polarisation) measurements are made using a 150 nm diameter nanopipet probe filled with aqueous sulfuric acid (pH 2.3), over a polycrystalline body centred cubic (bcc) low carbon steel surface. Used widely as a construction material, low carbon steel is both relatively cheap and easily manufactured into particular shapes without splitting or wrinkling [34]. Acidic solutions, such as the sulfuric acid investigated herein, are commonly used to remove scales and corrosion products from carbon steels, however without the extensive use of inhibitors, these cleaning processes can also have a detrimental impact (*i.e.*, corrosion) on the condition of the steel surface [35]. By combining the spatially-resolved electrochemical data from SECCM with structural information from electron backscatter diffraction (EBSD) and scanning transmission electron microscopy (STEM) in the same areas as the electrochemical measurements, microscopic structure (*e.g.*, crystal orientation) is shown to play an important role in modulating the corrosion susceptibility of low carbon steel. We attempt to rationalise these observations by complementary density functional theory (DFT) calculations.

2. Experimental

Electrode material and chemical reagents. The substrate used in this study was a low carbon steel, the chemical composition of which is presented in Table 1. The samples, of size 5 × 21 mm, were mounted in a conductive mounting compound (KonductoMet. Buehler, U.S.A) using a mounting press (SimpliMet. Buehler, U.S.A). Samples were then polished on a polishing cloth (TriDent. Buehler, U.S.A) with a polishing machine (AutoMet 3000 Pro. Buehler, U.S.A) using 9 μm, 3 μm and 1 μm polishing suspensions followed by a final polish using 0.05 μm alumina suspension (MasterPrep Alumina. Buehler, U.S.A) on a different cloth (MicroCloth. Buehler, U.S.A). To remove contamination from polishing suspensions, samples were cleaned with acetone, soapy water and then deionised water before being blown dry. Sulfuric acid (H_2SO_4, Merck, 96%) was used as supplied. All solutions were prepared with ultrapure deionised water (Integra HP, Purite, U.K.), which has a resistivity of 18.2 MΩ cm at 25 °C.

Surface characterisation. SEM and EBSD characterisation was carried out with a Zeiss SUPRA FE-SEM (Zeiss, Germany), using a Nordlys EBSD detector (Oxford Instrument, U.K.). SEM images and EDS data were collected at 10 keV, whereas EBSD images were collected at 20 keV, with the sample tilted at 70° to the detector. Following EBSD characterisation, grains that were chosen for study were either on or close to the low index orientations, (100), (101) and (111). Criteria set in this study was 10° deviation from the desired orientation.

Before TEM analysis, the sample was first extracted from the surface with focussed ion beam (FIB) milling using a ThermoFisher Scientific Scios DualBeam (ThermoFisher, U.S.A). In brief, an area of the surface chosen for examination was coated by a Pt layer to protect the area from damage. The regions surrounding this area were then subjected to a beam of Ga ions which effectively milled through the surface. Before removal, the examination area was attached to a tungsten rod with the use of deposited Pt, and once attached, the area was then cut free from the surface. The extract was then attached to carbon coated copper TEM grid, again with the use of deposited Pt. The extract was then 'thinned' with the Ga ion beam until a cross section of the SECCM scanning site was clearly visible. STEM was subsequently carried out on the thinned sample with a ThermoFisher Talos F200X FEG (ThermoFisher, U.S.A).

SECCM probe fabrication. Borosilicate capillaries (GC120F-10. Harvard Apparatus, U.S.A) were mounted on a laser puller (P-2000. Sutter Instruments, U.S.A) and pulled to give an opening diameter of approximately 150 nm at the end of the pipet (as confirmed by FE-SEM). Pulling parameters: Line 1: HEAT 350, FIL 3, VEL 30, DEL 220, PUL -; Line 2: HEAT 350, FIL 3, VEL 40, DEL 180, PUL 120. The pulled pipet was then filled with 5 mM H_2SO_4, producing a droplet at the tapered end. Silicone oil (Fluka Analytical) was used to

Table 1
Chemical composition of the low carbon steel determined using energy dispersive X-ray spectroscopy.

%	C	Mn	Si	Cr	Al	P	S	Cu
Low Carbon Steel	0.05	0.3	<0.03	0.06	0.03	<0.02	<0.02	0.04

reduce evaporation of the solution from the back of the nanopipet by placing a small amount on top of the sulfuric acid solution, as previously utilised [23,33]. A Pd/H_2 quasi reference counter electrode (QRCE) was then inserted into the electrolyte which were prepared by hydrogenating palladium wire, of thickness 0.125 mm, in 50 mM sulfuric acid solution. The Pd/H_2 QRCE was calibrated, as the open circuit potential measured against a commercial Ag/AgCl reference electrode (ET072-1, eDAQ, Australia), in 5 mM H_2SO_4 using a CHI400 potentiostat (CH Instruments Inc., U.S.A).

SECCM configuration. The SECCM set up is shown schematically in Fig. 1a, which has been discussed in greater detail previously [30,33]. The nanopipet was mounted on a *z*-piezoelectric positioner (P-753.2 LISA. PhysikInstrumente, Germany) which was then positioned near to the surface manually with a micropositioner. The sample stage was placed on top of a *xy*-piezoelectric positioner (P-621.2 PIHera, PhysikInstrumente) for fine horizontal movement. As the nanopipet was approached to the surface automatically (at 3 μm/s), a voltage (0.563 V vs Ag/AgCl) was applied to the QRCE so that a surface current (i_{surf}) was detected once the droplet had made contact with the substrate. This surface current response was used as the feedback parameter to halt the approach. The threshold used during approach was set at *ca.* 2 pA for this study. Note that the nanopipet itself did not make contact with the surface.

Upon contacting the substrate surface via the nanopipet meniscus, a potentiodynamic polarisation experiment was performed by sweeping the potential at the QRCE from 0.563 to −1.437 and back to 0.563 V vs Ag/AgCl and the resulting surface current was recorded. Data points were recorded as an average of 128 samples taken every 4 μs (*i.e.*, approximately every 0.5 ms). After the experiment for each scanning point had concluded, the nanopipet was then retracted from the surface (at 10 μm/s) and moved automatically to the next scanning site defined by the hopping distance. The process was repeated over a grid of scanning sites to map the electrochemical response of the surface.

Mass-transport in the nanopipet orifice is similar to the spherical diffusion at ultramicroelectrodes due to contribution of the radial component in the tapered capillary [36]. Steady-state conditions are thus established rapidly during measurements (*vide infra*) and the solution composition at the tip orifice is re-set to the bulk composition between each successive meniscus landing in a new location, due to rapid diffusional exchange between the end and the bulk of the nanopipet [37]. Note, further, that the anodic dissolution of iron is independent of the Fe^{2+} concentration in solution [38]. Although SECCM measurements are made on a much more rapid timescale than classical corrosion measurements, SECCM studies identify electron-transfer kinetics at different active sites, and are thus pertinent to understanding corrosion processes.

The entire SECCM apparatus was mounted on an optical table (RS2000. Newport, U.S.A) supported on vibration isolation supports (S-2000. Newport, U.S.A). The set up was also shielded with a Faraday cage equipped with heat sinks and vacuum panels to minimise noise and variations in temperature. The QRCE potential was controlled with respect to ground and the current flow at the substrate was measured using a home-built electrometer. Data acquisition and fine control of all instrumentation was achieved using an FPGA card (PCIe-7852 R) controlled by a LabVIEW 2016

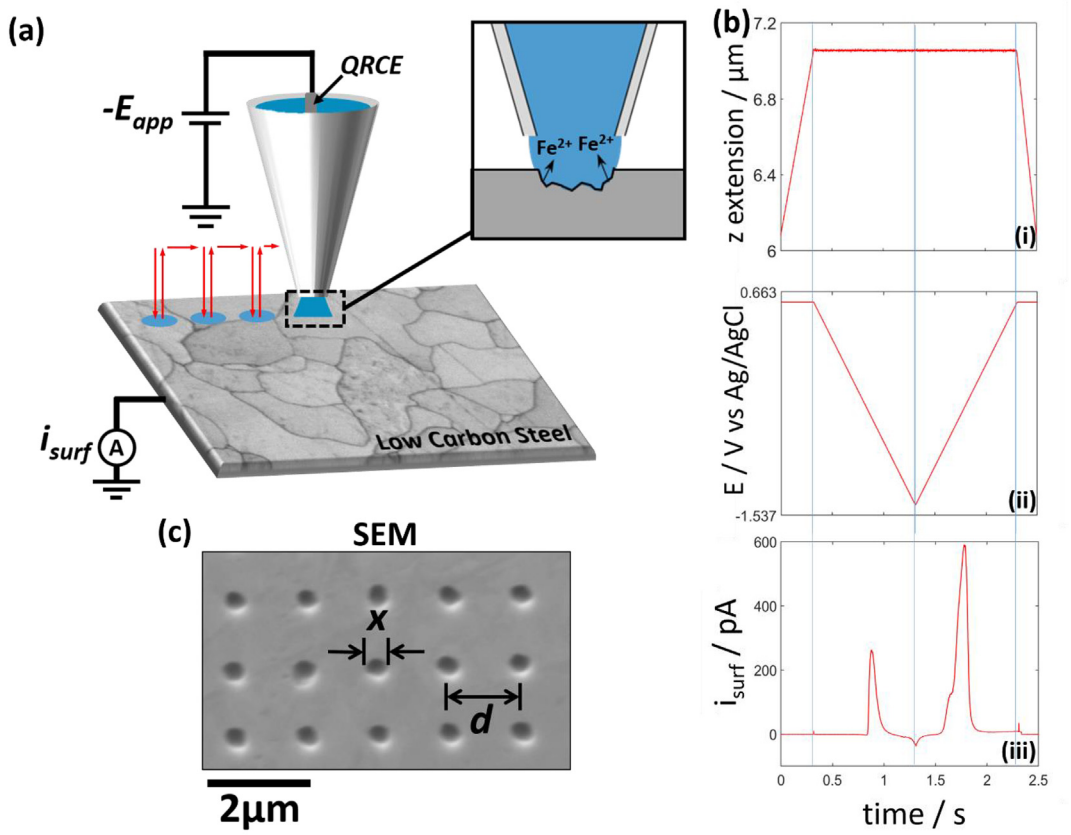

Fig. 1. **(a)** Schematic of the voltammetric hopping-mode protocol of SECCM, used herein. The direction of motion by the probe is indicated by the red arrows. In this study, the nanopipet was filled with 5 mM H_2SO_4 and equipped with a Pd/H_2 QRCE. **(b)** Plots of **(i)** z-extension, **(ii)** applied potential, *E*, **(iii)** surface current, i_{surf}, during a single "hop" of a voltammetric SECCM experiment (voltammetric scan rate, $\upsilon = 2\ V\ s^{-1}$). **(c)** SEM image taken of the low carbon steel surface, showing 15 individual droplet "footprints", after an SECCM scan. The nanopipet diameter was 150 nm, the hopping distance, *d*, between pixels was 1.2 μm and the droplet "footprint" diameter, *x*, for each measurement was measured as ≈450 nm. (For interpretation of the references to colour in this figure legend, the reader is referred to the Web version of this article.)

(National Instruments, U.S.A) interface running the Warwick Electrochemical Scanning Probe Microscopy (WEC-SPM, www.warwick.ac.uk/electrochemistry) software.

Software and data processing. The experimental data was processed using the Matlab R2016b (Mathworks, U.S.A) and OriginPro 2016 64bit (OriginLab, U.S.A) software packages. The possible identity of the corrosion products formed during SECCM (and observed with STEM imaging) was calculated using the HYDRA and MEDUSA software package (KTH, Sweden) [39], which considers the thermodynamically stable species (*i.e.*, at equilibrium) that may exist under a given experimental condition. The following solid (iron oxysulphate) corrosion products were predicted: $Fe(OH)_2$, $FeSO_4{\cdot}7H_2O$, $Fe_2(SO_4)_3$, Fe_2O_3, FeOOH and $H_3OFe_3(SO_4)_2(OH)_6$.

Density function theory calculations. The Quantum Espresso [40] software toolbox was used to perform plane wave basis set Kohn-Sham Density Functional Theory (DFT) [41] calculations with ultrasoft pseudopotentials [42]. Pseudopotentials were all taken from the PSLibrary, version 1.0 [43]. A plane-wave kinetic energy cut-off of 800 eV was found to converge binding energies to at least 2 significant figures (in eV units). A Monkhurst-Pack grid of $4 \times 4 \times 1$ *k*-points with no origin shift [44] was found to be adequate to converge energies with respect to Brillouin zone sampling.

Slab models of (100), (101) and (111) Fe planes with a finite thickness of 5 layers were employed to model Fe dissolution energies. A vacuum gap of 7 Å on both sides of the slab in the *z*-direction was used to simulate open boundary conditions. Additionally, any remaining spurious interactions through the *z*-boundary were corrected using the Martyna-Tuckerman dipole correction scheme [45] as implemented in the Environ model [46,47]. The solvation model was used to account for solvent interaction energy terms between the surface and the solvent and between the dissolved iron and the solvent. To parameterise the continuum solvent model for water, the parameters suggested previously [46,47] were used. This was found to converge the surface energies down to 0.001 eV error.

First, a variable-cell geometry optimisation of the bulk metal cell was performed to find a converged lattice parameter. In the case of hcp crystal structure of Fe, these were a = b = c = 2.71177 Å. Slabs formed from the bulk metal were used in a fixed-cell geometry optimisation constraining the position of the two layers furthest from our simulated surface to calculate the bare surface energy in vacuum (E_{bV}) and in solvent (E_{bS}).

A single layer of Fe atoms was manually removed from the surface. The following equation was used to compute binding energies of the Fe layer (E_{Fe-Fe}):

$$E_{Fe-Fe} = \frac{1}{N}\left(E_{bS\_n(layers)} - E_{bS\_n-1(layers)} - N \times E_{Fe^{2+}}\right) \quad (1)$$

where $E_{Fe^{2+}}$ refers to the energy of a Fe^{2+} cation in the centre of a solvent box, with the same parameters used for the slab calculations. Normalisation by the number of atoms (N) in a layer (n) was used to account for packing densities of individual grains.

An electronic energy convergence tolerance of 2×10^{-6} eV was used throughout these calculations. A Broyden charge density mixing [48] scheme, with local Thomas-Fermi screening [49] and Gaussian electronic smearing, with a smearing width of 0.1 eV were used to account for the metallic nature of our systems. We used the BFGS geometry optimisation scheme [50] with tolerances of 2×10^{-5} eV per atom in energy, 0.05 eV per in maximum force, 0.002 Å in maximum atomic displacement and in the case of the variable-cell, bulk geometry optimisation, 0.1 GPa maximum stress.

3. Results and discussion

SECCM: Operational Principles. The previously reported [29,30] voltammetric hopping-mode SECCM protocol used in this study is shown in Fig. 1a. A single-channel nanopipet of diameter ≈150 nm, filled with 5 mM H_2SO_4 (pH = 2.3) and equipped with a palladium-hydrogen ($Pd-H_2$) QRCE, which possessed a potential of 0.437 V vs Ag/AgCl (3.4 M KCl), was employed to perform spatially-resolved potentiodynamic polarisation measurements. The *z*-position of the nanopipet probe, applied potential and surface current (i_{surf}) measured synchronously during a single "hop" of an SECCM scan is shown in Fig. 1b. During approach of the nanopipet probe to the surface (*i.e.*, extension in the *z*-direction at 3 μm/s, herein, Fig. 1b–i), a potential (0.563 V vs Ag/AgCl, herein, Fig. 1b–ii) was applied between the QRCE and the surface (working electrode), such that when the meniscus (droplet) protruding from the end of the probe initially made contact with the surface, a current (i_{surf}) flowed at the substrate surface (in a 2-electrode cell), as the circuit was closed (Fig. 1b–iii). This was used as a feedback signal (set point) to instantaneously halt the approach of the nanopipet, so that it did not contact the surface. Upon meniscus landing, a local potentiodynamic polarisation experiment (between 0.563 V and −1.437 V vs Ag/AgCl at 2 V s^{-1}, herein) was performed, before the probe was retracted and moved to a new site (pixel) with a predetermined hopping distance, *d* (*vide infra*).

The potential applied between the QRCE and the surface during the approach (0.563 V vs Ag/AgCl) was well within the passive region, where a protective passive (oxide) film was formed, for example, via the reaction:

$$2Fe + 3H_2O \rightarrow Fe_2O_3 + 6H^+ + 6e^- \quad (2)$$

Thus, the Fe surface in contact with the meniscus would be passivated rapidly upon each meniscus landing. Once contact was established between the droplet and the surface, the potential was swept cathodically to enter the active region, where the protective passive film is removed (reduced) and the iron dissolution reaction occurs:

$$Fe \rightarrow Fe^{2+} + 2e^- \quad (3)$$

As mentioned above, an advantage of nanoscale electrochemical measurements is that steady-state conditions are established rapidly, which means that relatively fast voltammetric sweep rates, such as 2 V s^{-1} used here, can be applied [36,37]. Indeed, we have shown that under such conditions, SECCM measurements provide highly relevant data for understanding electron-transfer kinetics relevant to corrosion phenomena, as highlighted by the clear grain contrast in activity seen in electrochemical movies (SI, Movie 1). As a rule of thumb, the time to steady-state in SECCM is *ca.* $t_{ss} \sim (10a)/D$, where a is the tip radius and D is the diffusion coefficient of Fe^{2+} [51]. Thus, for the studies herein, with $a = 75$ nm and D ~10^{-5} cm^2 s^{-1}, t_{ss} ~1 ms [36,37]. Note that a smaller voltammetric scan rate would lengthen the time to record datasets and cause more extensive local damage to the surface due to prolonged anodic dissolution at each spot (which would also expand the spot area). The ability to apply fast scan rates is advantageous in terms of limiting the perturbation of the surface.

Continuing the potential sweep into the cathodic region, the oxygen reduction reaction (ORR), Eq (4), and (to a more appreciable extent) hydrogen evolution reaction (HER), Eq (5), occur:

$$O_2 + 4H^+ + 4e^- \rightarrow 2H_2O \quad (4)$$

$$2H^+ + 2e^- \rightarrow H_2 \quad (5)$$

Once the cathodic potential sweep was completed, the cycle was then reversed and the potential was swept anodically. Corrosion is a dynamic process and, as a result, the working electrode (low carbon steel) surface changes irreversibly (physically and chemically) during active dissolution. For this reason, the potential was swept from anodic to cathodic domains and only the processes occurring before (*i.e.*, in the passive region) and in the active region during the forward potential sweep have been considered herein (*vide infra*).

The result of a voltammetric hopping mode experiment on the surface of low carbon steel (using the cyclic potentiodynamic polarisation protocol outlined above) is demonstrated in Fig. 1c, where each spatially-independent measurement site is seen as an array of droplet "footprints" by using scanning electron microscopy (SEM). A full matrix of the droplet footprints ($60 \times 60 = 3600$ measurements) visible in SEM after SECCM experiments can be found in the Supporting Information, Fig. S1. The diameter of the footprints, x, defining the "working electrode area" during each measurement is consistent from point-to-point ($\approx$450 nm). The ultimate spatial-resolution of the scan is determined by d, which was conservatively set to 1.2 μm herein to ensure that each potentiodynamic polarisation measurement was independent of the last.

Spatially-resolved potentiodynamic polarisation experiments on low carbon steel. In order to ascertain the structure-dependence of the anodic processes (iron dissolution) on low carbon steel, a 72×72 μm^2 (60×60 pixel^2) voltammetric SECCM scan was carried out. The potentiodynamic polarisation curve (only forward sweep considered, *vide supra*) obtained by averaging all scanning points (3600 total) is shown in Fig. 2a. A simplified Pourbaix diagram for pure iron (considered to be representative of the investigated low carbon steel, see Table 1) is also included in Fig. 2b to indicate the predicted thermodynamically stable species throughout the potential sweep [52]. The low carbon steel surface is initially in a passive state (labelled as ①, Fig. 2b) from 0.563 V vs Ag/AgCl through to *ca.* −0.24 V, where a small reduction peak (cathodic current) is observed (inset in Fig. 2a), attributable to passive film reduction (labelled as ②, Fig. 2b):

$$Fe_2O_3 + 6H^+ + 2e^- \rightarrow 2Fe^{2+} + 3H_2O \quad (6)$$

The charge passed during this process was calculated to be 20 ± 2 pC, which corresponds to a thickness of ~8 ± 1 nm, assuming an Fe_2O_3 film. Following the reduction peak, in the potential range *ca.* −0.49 V to −0.94 V (active region), iron dissolution (Eq (3)) is the dominant process (labelled as ③, Fig. 2b), giving rise to large oxidation currents (peaking at $\approx$290 pA, which corresponds to a current density of $\approx$0.2 A cm^{-2}). The oxidation peak (at −0.587 V) is formed as the increasing corrosion rate resulting from the removal of the protective passive film (Eq (6)) is balanced by the decreasing driving force for iron dissolution (Eq (3)), as the potential is swept cathodically. Note that due to the fine tip geometry (diameter of $\approx$150 nm) and relatively dilute supporting electrolyte (5 mM H_2SO_4), ohmic (iR, where R is the tip resistance, calculated to be 320 MΩ, herein) drop is on the order of $\approx$90 mV at the oxidation peak. Although this may distort the shape of the potentiodynamic polarisation curve to an extent, it does not affect grain-dependent trends in i_{surf}, considered in detail below. Upon sweeping to potentials negative of −0.937 V, the surface current is dominated by cathodic processes (labelled as ④, Fig. 2b), where iron re-deposition occurs (reverse of Eq (2)), in addition to cathodic (electrocatalytic) processes such as the ORR, Eq (3), and (predominantly) HER, Eq (4). This behaviour is consistent with the macroscopic electrochemical response of similar iron-based materials in acidic media [1].

Selecting four characteristic potentials (0.063, −0.547, −0.587, −1.437 V vs Ag/AgCl, labelled in Fig. 2a), spatially-resolved i_{surf} maps are shown in Fig. 2c. Comparison of Fig. 2c with the co-located EBSD map in Fig. 2d reveals that: (i) tens of potentiodynamic polarisation experiments (*ca.* 20 to 50) are carried out on each grain, statistically validating our inferences below; and (ii) some processes appear to be grain-dependent, while others are grain-independent. Starting in the passive domain ($E_{app} \approx$ 0.563 to −0.237 V vs. Ag/AgCl, Fig. 2c–i), the low current values in the i_{surf} map do not show discernible features related to the underlying crystal structure. Although this may suggest that the resistivity/protectiveness of the passive film is grain-independent, the i_{surf} values measured in this region are dominated by the background noise (*ca.* 2 pA peak-to-peak, detailed in the Experimental Section), and thus it is likely that any differences between the grains are too minute to detect.

In the active domain ($E_{app} \approx$ −0.487 to −0.937 V vs. Ag/AgCl, Fig. 2c-ii and 2c-iii) there is a clear relationship between crystal orientation (Fig. 2d) and the rate of iron dissolution, evidenced by grain-dependent i_{surf} values (*vide infra*). In the cathodic region (Fig. 2c–iv), where the HER is expected to be the dominant process [53], i_{surf} shows a weaker grain-dependence. As discussed above, the preceding anodic processes are expected to have a significant influence on the processes occurring in the cathodic region due to physical changes to the surface (*e.g.*, surface dissolution and deposition of corrosion products) and compositional changes to the surface and electrolyte (*e.g.*, the formation of soluble Fe^{2+} species within the droplet cell), and Fig. 2b–iv is thus difficult to interpret. Note that in a companion study [54], we have employed a potential-pulse waveform (*i.e.*, chronoamperometry) to reveal the structure-dependence of the HER on low carbon steel in aqueous sulfuric acid (pH 2.3), and this is a better means of elucidating HER kinetics. As such, we do not consider the HER process any further here, but focus on the anodic dissolution of Fe (*vide infra*).

Taking all of the i_{surf} maps (every 2 mV) over the entire potential range (0.563 to −1.437 V vs Ag/AgCl), a spatially-resolved i_{surf}–E movie was constructed, shown in the Supporting Information, Movie S1. Note that throughout the movie, a small number of individual pixels appear to be far more active than the rest, which are labelled in Fig. 3a and further examined (*i.e.*, pixel-resolved i–E curves shown) in detail in Fig. 3b. For these "active pixels", the onset potential for active dissolution is *ca.* 100 mV (95–125 mV) more positive, and the anodic peak currents are larger (312–836 pA) compared to the surface average i–E curve (black trace, peak current of 290 pA). Multiple processes appear to contribute to the anodic current, giving rise to a "split peak", with the process occurring at more positive potentials giving rise to unstable current fluctuations (also seen in the passive region, at $E > 0.2$ V vs Ag/AgCl). These additional processes are thought to arise from the oxidation (and dissolution) of manganese sulfide (MnS) inclusions, which has been addressed in our previous study [33], highlighting MnS inclusions as possible initiation sites for localised corrosion. Under anodic dissolution conditions, the presence of MnS inclusions cannot be confirmed with EDS, after experiments, as the inclusions undergo partial or complete dissolution as the potential sweeps through the active region. However, SEM images after experiments (*e.g.* Fig. 3c and d) shows a larger deposit of corrosion products and/or greater damage to the surface at these "active pixel" sites.

Supplementary data related to this article can be found at https://doi.org/10.1016/j.electacta.2019.135267.

Movie S1 and Fig. 2c–ii convincingly show that electrochemical iron dissolution is influenced by surface structure (*i.e.*, crystallographic orientation), which is further explored in Fig. 4. Three characteristics of the anodic peak are considered, labelled in Fig. 4a:

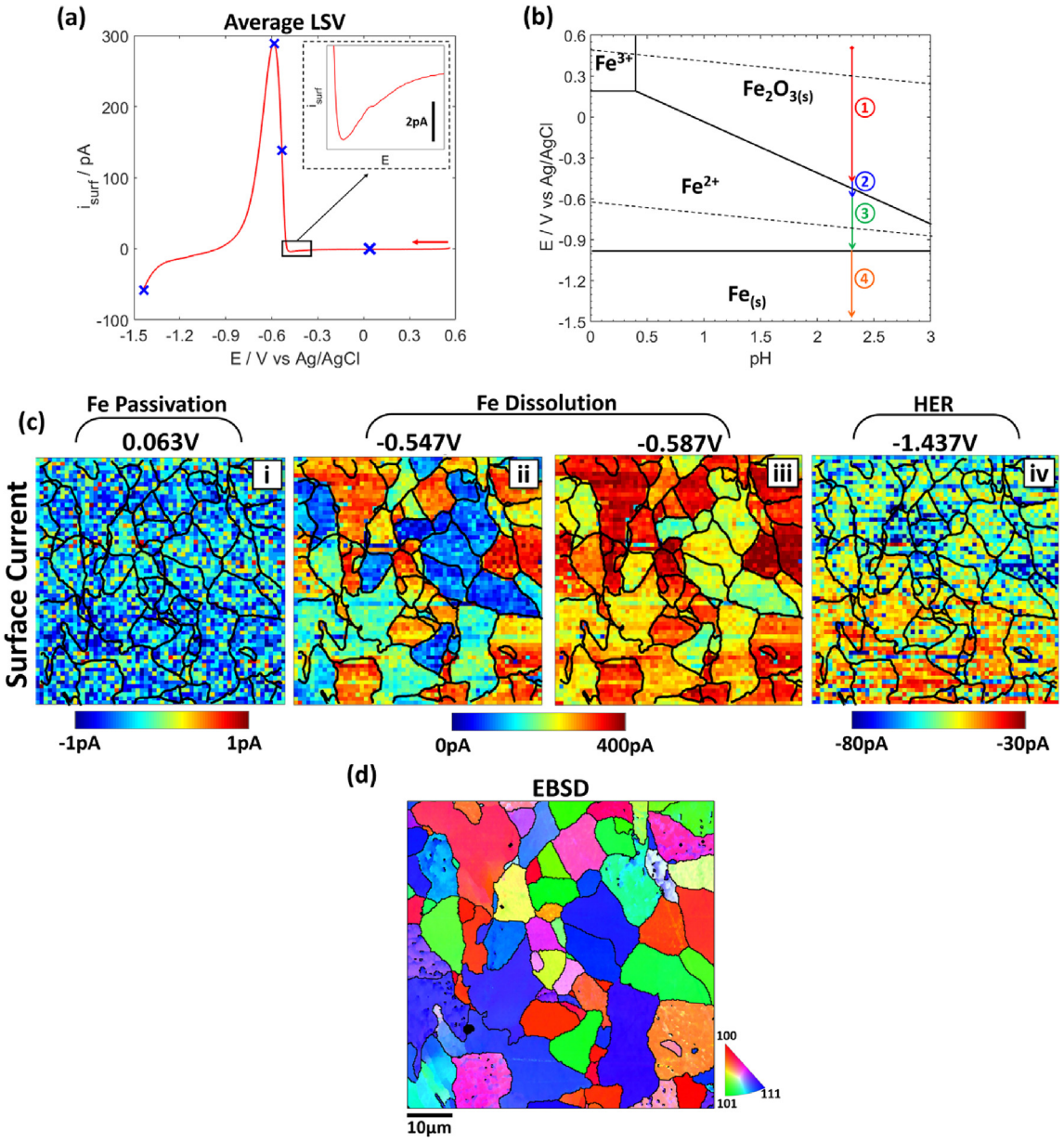

Fig. 2. **(a)** Potentiodynamic polarisation (i–E) curve ($\upsilon = 2$ V s^{-1}), obtained by averaging the forward sweep of 3600 (60 × 60 pixel^2 covering 72 × 72 µm^2) individual measurements on a low carbon steel sample. The nanopipet was ≈150 nm in diameter and filled with 5 mM H_2SO_4. **(b)** Simplified Pourbaix diagram for Fe. Coloured arrows indicate the potential range covered by the potentiodynamic polarisation curve in (a) at pH 2.3, with the numbers on the plot corresponding to the following: ① passive film formation, ② passive film reduction, ③ active iron dissolution and ④ cathodic processes (HER and ORR). **(c)** Spatially-resolved i_{surf} maps obtained at **(i)** 0.063 V **(ii)** −0.587 V **(iii)** −0.547 V and **(iv)** −1.437 V vs Ag/AgCl [indicated on the corresponding average i–E curve in (a)]. Note the different current scales. **(d)** Corresponding EBSD map, showing the crystallographic structure of the area scanned with SECCM in (c).

the reduction pre-peak potential (V_p^{red}); the oxidation peak current (i_p); and the oxidation peak potential (V_p^{ox}), maps of which are shown in Fig. 4b, c, and d, respectively. The charge passed during oxidation (Q^{Ox}), which is proportional to the amount of iron dissolved during oxidation and; the full width half maximum of the oxidation peak (*FWHM)*, which indicates the range of potentials over which active dissolution occurs, are also presented in the Supporting Information, Fig. S2. Other areas of the low carbon steel surface were also mapped using the same SECCM protocol; examples of the spatially-resolved i_p maps are plotted alongside co-located EBSD maps in the Supporting Information, Fig. S3, to highlight the reproducibility of the method.

The cathodic process prior to the active region (signified by V_p^{red}) is attributable to the reduction of the passive film (Eq (5)), which leaves the unprotected low carbon steel surface exposed for active dissolution. In other words, V_p^{red} indicates the potential above which the passive film is stable, or conversely, below which active dissolution will occur. Clearly, the grain-dependence of V_p^{red} indicates that the nature of the passive film, formed during the passive region of the potential sweep, varies between crystallographic facets. This may arise due to variations in the thickness and/or structure of the passive film, both of which could perceivably lead to differing film reduction behaviour. The anodic peak, the position (V_p^{ox}, Fig. 4d), magnitude (i_p, Fig. 4c),

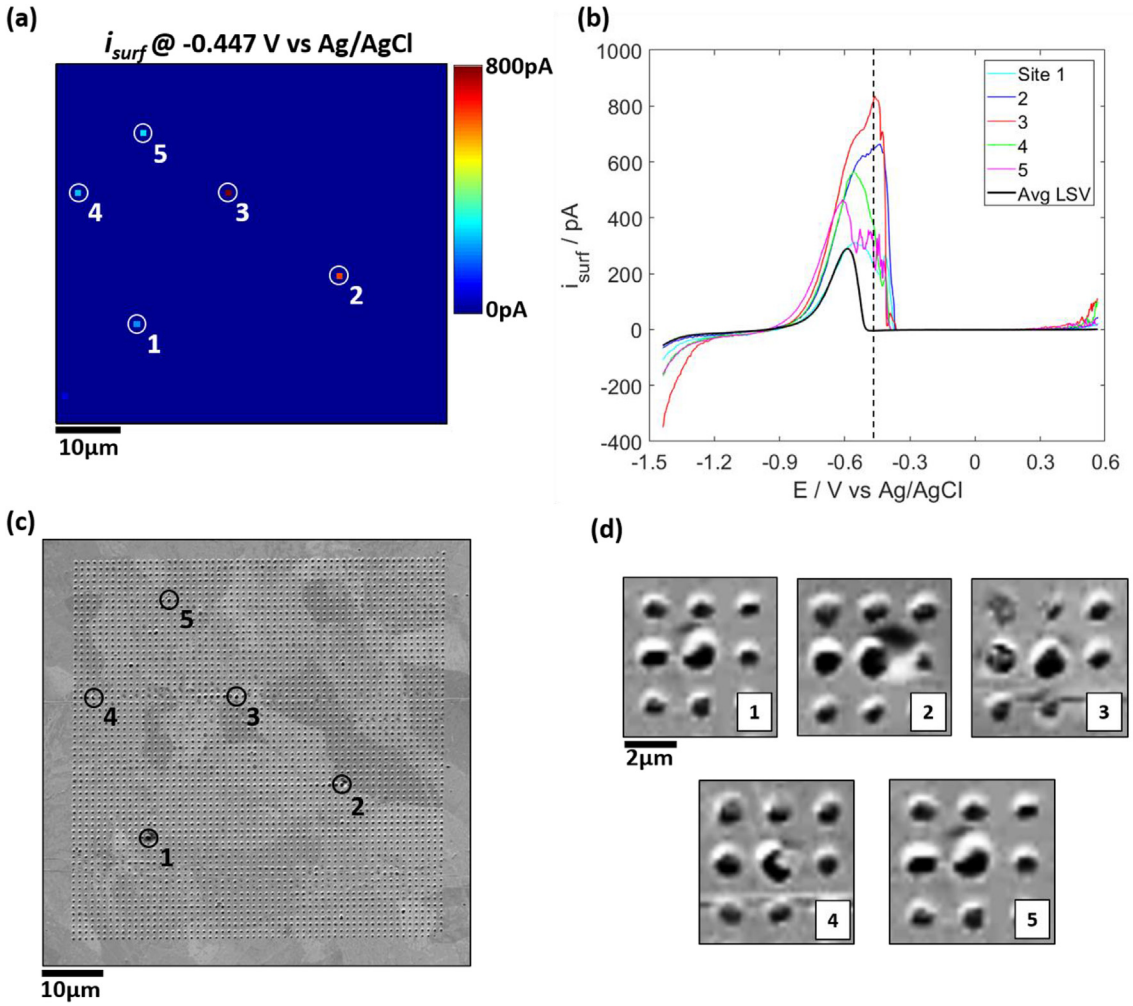

Fig. 3. **(a)** Spatially-resolved i_{surf} map obtained at a potential of −0.447 V vs Ag/AgCl QRCE using the voltammetric SECCM configuration. The i_{surf} maps comprise 3600 pixels (60×60 pixels^2) over a 72×72 µm^2 area, obtained with a nanopipet probe of diameter ≈ 150 nm containing 5 mM H_2SO_4. **(b)** i–E curves ($\upsilon = 2$ V s^{-1}) obtained from the 5 highly active pixels (coloured traces) labelled in (a) versus the average response (black trace) obtained from the 3600 pixels across the surface. **(c)** Scanning electron microscopy (SEM) image of corresponding area scanned with SECCM shown in (a). **(d)** Zoomed-in SEM images of the "active pixels" (the centre spot of each 3×3 array of spots) indicated in (a) and (c).

charge passed (Q^{Ox}, taken as the integral of the peak, see Supporting Information, Fig. S2), width (taken as the full width at half maximum, FWHM, see Supporting Information, Fig. S2) are all grain-dependent. Comparing the maps, the grains that possess passive films that are easiest to reduce (most-positive V_p^{red}, Fig. 2b) undergo the highest rates of dissolution (highest i_p, Fig. 2c) over the widest potential range (largest FWHM, Fig. S2c).

Grain dependent anodic iron dissolution at low carbon steel. In order to gain an insight into which grains facilitate anodic iron dissolution and further explain these dependencies, we focus on the grains of low-index crystal orientation [*i.e.*, the (100), (101) and (111) crystal facets]. All grains within 10° of the (100), (101) and (111) orientations are shown in Fig. 5a–i, ii and iii, respectively, and average potentiodynamic polarisation curves obtained from each of the grains are shown in Fig. 5b. In total, 130, 264 and 365 individual measurements were taken on the (100), (101) and (111) grains, respectively. Evidently, from Fig. 5b, the variation in the potentiodynamic polarisation curves within a family of grains [*i.e.*, compare the red curves for (100)] is much less than that between families of grains [*i.e.*, compare the red and green curves for (100) and (101), respectively], demonstrating the strong crystallographic-dependence of anodic iron dissolution. The average LSVs also show that the difference in dissolution current between grains is greater on the right hand side of the oxidation peak compared to the left hand side. In other words, sweeping the potential from positive to negative, the potential at which anodic iron dissolution initiates (*e.g.*, Figs. 4b and 5b, inset) is more strongly grain-dependent than the potential at which iron dissolution ceases.

V_p^{red} increases in the order (101) < (111) < (100), from which it can be inferred that the passive (oxide) film is the thinnest and/or least protective on the (100) grains. This grain-dependent film composition/structure is consistent with previous studies, where it has been shown that the oxide films electrochemically grown on the (100) and (110) crystal facets of iron have different crystallographic structures [55]. Taking i_{surf} at −0.581 V vs Ag/AgCl as an indicator of the relative rates of iron dissolution in the active region, histograms were constructed from the grain-resolved potentiodynamic polarisation curves, shown in Fig. 4c. Note that −0.581 V vs Ag/AgCl (indicated in Fig. 4b) was chosen to minimise the influence from the protective passive film (assumed to be completely removed at *ca.* 100 mV more negative than V_p^{red}) and cathodic processes. Average i_{surf} values increase in the order 218 ± 23, 252 ± 22, and 334 ± 26 pA (mean ± standard deviation) for the (101), (111) and (100) facets, respectively, which follows the same

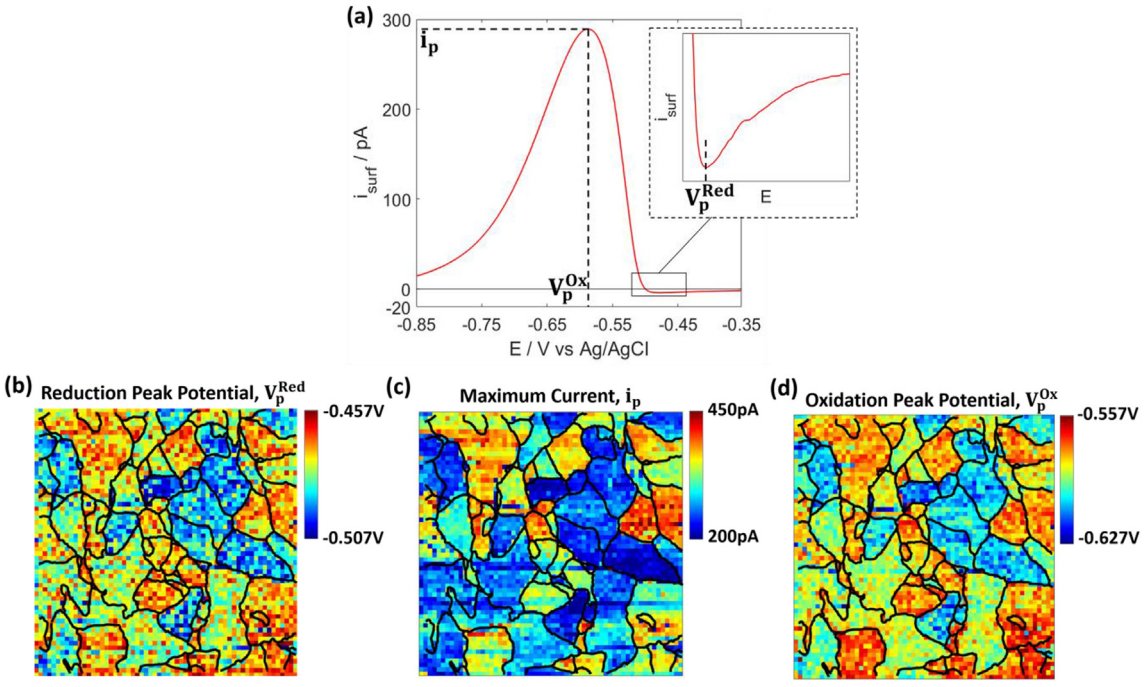

Fig. 4. **(a)** i–E curve ($\upsilon = 2\,V\,s^{-1}$), obtained by averaging the forward sweep of 3600 (60×60 pixel^2 covering $72 \times 72\,\mu m^2$) individual measurements on a low carbon steel, performed in the voltammetric hopping mode SECCM configuration. The nanopipet was $\approx$150 nm in diameter and filled with 5 mM H_2SO_4. The reduction peak potential, V_p^{Red}, oxidation peak potential, V_p^{Ox}, and oxidation peak current, i_p, are labelled on the plot. Spatially-resolved maps of **(b)** V_p^{Red}, **(c)** i_p and **(d)** V_p^{Ox}.

trend as V_p^{red}, above. Higher values of V_p^{red} and i_{surf} in the active region indicate greater corrosion susceptibility, which increases in the order: (101) < (111) < (100).

In a previous study on iron, the grain dependence of iron dissolution was studied with atomic force microscopy (AFM), where it was shown that the (100) grains exhibited the largest dissolution rate during electropolishing in acidic media at a constant current density of 0.3 A cm^{-2}. In a different study on iron single crystals in pH 1 sulfuric acid, it was also found that the dissolution rate for the low index planes increased in the sequence (100) > (111) > (101) [56]. Our results, using a different approach, are consistent with this prior work. Furthermore in a study carried out on a light weight ferritic steel, an EDC technique revealed a critical current density (*i.e.*, maximum current during active dissolution) that was *ca.* 50% larger at (100) grains compared to the (111) orientation (compared to *ca.* 31%, herein) in 0.5 M H_2SO_4. Although the material studied herein (low carbon steel) was different to those considered [3,8], these studies lend weight to our observation of higher active dissolution currents on the (100) grains compared to the (101) or (111) grains.

There is much speculation in the literature as to why grains exhibit different anodic dissolution rates. For example, it has been theorised [8] that the surface density of the atoms of each grain governs corrosion susceptibility/resistance (also applied to other metals, such as magnesium [57]), where anodic metal dissolution rates decrease with increasing packing density (*i.e.*, densely packed surface atom layers 'shield' the sub-surface layers from interaction with the corrosive electrolyte). For the case of ferrite steel (*i.e.*, the structure of low carbon steel), surface atom density increases in the order 1.2×10^{15}, 1.7×10^{15} and 1.9×10^{15} atoms cm^{-2} for the (100), (101) and (111) planes, respectively. While this certainly fits our observations for the (100) grains (Fig. 5b, red traces), such a naïve analysis cannot explain the higher rates of dissolution observed at the (111) compared to the (101) planes (Fig. 5b, blue and green traces, respectively). This suggests that there are likely other factors that affect the active dissolution rate of the individual grains, explored further below.

STEM inspection of individual SECCM scanning sites. To visualise the physical changes to the low carbon steel that occur during SECCM-induced anodic corrosion, FIB milling was used to extract a section of the surface containing individual scanning sites (*i.e.*, individual SECCM "pixels"). Note that a pipet probe of diameter $\approx$2 μm was used in this particular experiment to enable the more ready preparation of the cross-section. The step-by-step guide of the FIB milling procedure is shown in Fig. 6 and is also described in detail in the Experimental Section.

An STEM analysis of the cross-sectional structure and composition of a typical area where SECCM measurements were made is shown in Fig. 6c. There is a deep recess relative to the surrounding areas resulting from the removal of Fe^{2+} during the active dissolution process (Eq (2)). Corrosion products are re-deposited over the top of this site (highlighted with a dotted line, thickness of *ca.* 140 nm), producing a layer that contains iron, sulphur and oxygen (electron dispersive spectroscopy, EDS). The EDS map for platinum is included to identify the protective layer from the FIB milling procedure. These corrosion products are likely comprised of iron (II) and iron (III) oxysulfate species, as calculated with the HYDRA and MEDUSA software, which consider the thermodynamically stable (equilibrium) solid products under a given set of experimental conditions (further details can be found in the Experimental Section).

Density functional theory calculations. To explore the possible factors governing the grain-dependent iron dissolution rates, density functional theory (DFT) calculations were performed that consider the binding energies of iron atoms at the surface of a lattice. In brief, we consider the thermodynamic properties for each of the low index crystal planes by calculating the energy required to remove (ionise) one monolayer of iron using the following (simplified) equation:

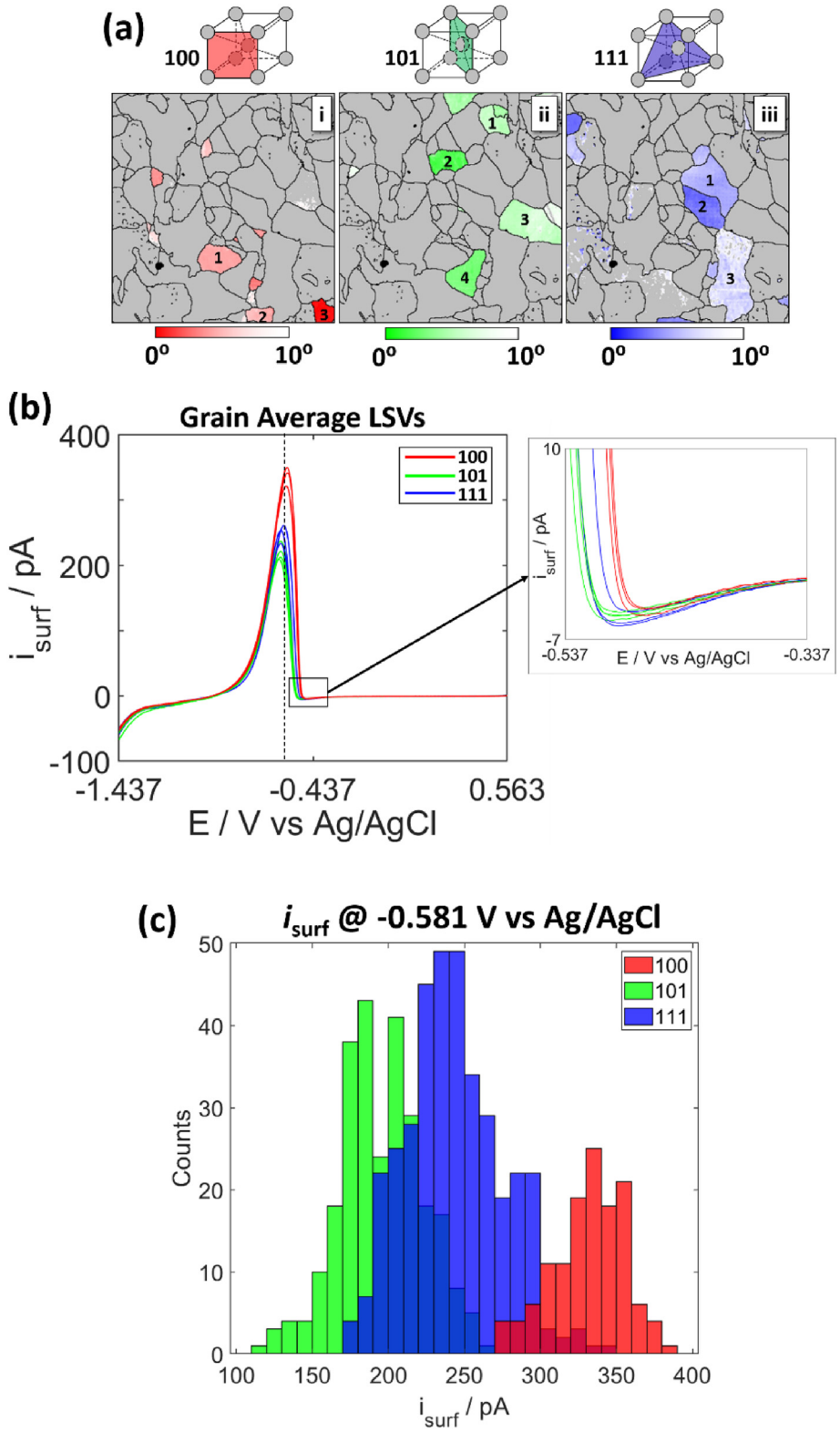

Fig. 5. **(a)** EBSD maps identifying the grains that have crystal orientations within 10° of the low index orientations, **(i)** (100), **(ii)** (101) and **(iii)** (111). **(b)** i–E curve ($\upsilon = 2\,V\,s^{-1}$) obtained by averaging the individual measurements performed on each of the low-index orientations [red = (100), blue = (111) and green = (101)], using the voltammetric hopping mode SECCM configuration. The nanopipet was ≈150 nm in diameter and filled with 5 mM H_2SO_4. **(c)** Distribution of i_{surf} measured at −0.581 V vs Ag/AgCl [indicated by dashed line on (b)] on each of the low index orientations. (For interpretation of the references to colour in this figure legend, the reader is referred to the Web version of this article.)

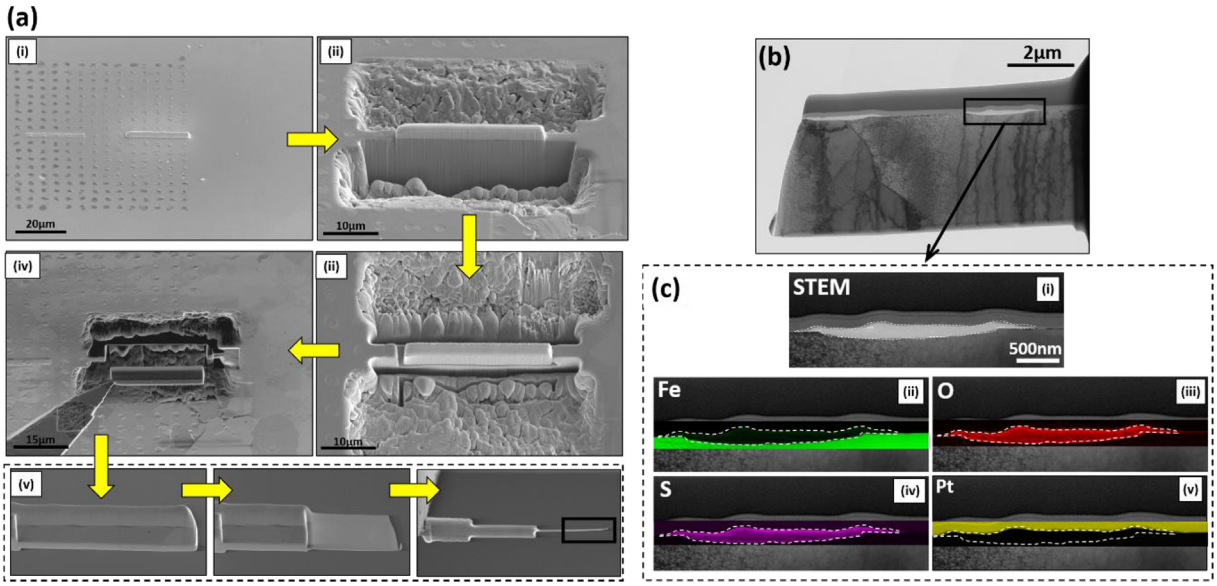

Fig. 6. **(a)** Step-by-step outline of the focussed ion beam (FIB) milling procedure used to extract single SECCM droplet "footprint" sites for cross-sectional analysis. **(i)** Covering the scanning site of interest with a protective platinum layer. **(ii)** and **(iii)** Ga ion beam milling around selected section. **(iv)** Removal of the extract from the low carbon steel matrix. **(v)** Thinning of the extracted section. **(b)** Cross-sectional scanning transmission electron microscopy (STEM) image of the extract. **(c)** (i) STEM image of the cross section of a droplet "footprint" (nanopipet diameter = 2 µm in this experiment), accompanied by corresponding EDS analysis for **(ii)** iron, **(iii)** oxygen **(iv)** sulphur, and **(v)** platinum.

$$E_{\mathrm{Fe-Fe}} = \frac{1}{N}\left(E_n - E_{(n-1)} - N \times E_{\mathrm{Fe}^{2+}}\right) \quad (7)$$

where $E_{\mathrm{Fe\text{-}Fe}}$ represents the binding energy of Fe on the surface of a particular plane, normalised by the number of atoms for a monolayer, E_{n} is the total energy stored in n monolayers of iron atoms, $E_{(\mathrm{n\text{-}1})}$ is the surface energy after removing one monolayer, $E_{\mathrm{Fe}^{2+}}$ is the energy of an Fe^{2+} ion liberated from the surface and N is the number of atoms per monolayer. Further details of the calculations can be found in the Experimental Section.

The measured i_{surf} values (at −0.581 V), 218, 252 and 334 pA scale with the calculated $E_{\mathrm{Fe\text{-}Fe}}$ values, −24.253, −24.237 and −24.216 eV for the (101), (111) and (100) planes, respectively (plot shown in the Supporting Information, Fig. S4). This means that crystal orientations where Fe atoms are thermodynamically easier to remove (and ionise), evidenced by less negative $E_{\mathrm{Fe\text{-}Fe}}$ values, correlate with higher active iron dissolution rates, evidenced by larger i_{surf} values at active potentials (Fig. 4). Note that the convergence error for each calculation was ±0.001 eV showing that despite the very subtle differences in energy between orientations, the calculations were sufficiently precise to confirm any trends between the dissolution behaviour of different crystal planes.

Dissolution of a crystalline solid in a solution is complex, involving a number of interacting processes in parallel at different characteristic sites [58,59]. Nonetheless, the above analysis suggests a correlation of the anodic dissolution kinetics with the free energy of ionization, consistent with a general semi-empirical framework for predicting dissolution rates based on free energy relations [58,60]. It must be emphasized that the DFT calculations are performed for a simplified system (*i.e.*, a plane of Fe atoms on a lattice, undergoing uniform dissolution/corrosion). The influence of anions (as well as other species present in solution) is not explicitly considered, which are known to influence the corrosion behaviour of steel, the most well-known example being Cl^- ions inducing localised (pitting) corrosion [61]. In reality, the grain-dependent corrosion susceptibility/resistance of low carbon steel is likely to be dependent on solution conditions [2] (*i.e.*, pH, electrolyte composition, *etc.*) which, as demonstrated herein, is amenable to analysis through SECCM, again highlighting the potential of this technique in corrosion research.

4. Conclusions

In this study, we have advanced the understanding of the dependence of anodic iron dissolution on the underlying crystallographic structure of low carbon steel in aqueous sulfuric acid (pH 2.3). This was achieved through the combination of local potentiodynamic polarisation experiments from SECCM (>100 measurements analysed on each low-index plane) with co-located structural information from EBSD, which revealed grain-dependent anodic iron dissolution rates that increase in the order (100) > (111) > (101). Local cross-sectional analysis with STEM imaging revealed a build-up of corrosion products within the dissolved area of an individual droplet "footprint" site, which was suggested to comprise insoluble iron oxysulfate species, formed during the active dissolution of iron. The grain-dependent anodic dissolution rates derived from SECCM were rationalized through complementary DFT calculations, which showed that the rate of iron dissolution, and hence corrosion susceptibility, increases with increasing (*i.e.*, less-negative) $E_{\mathrm{Fe\text{-}Fe}}$ values (*i.e.*, the energy required to remove a monolayer of iron from the surface of a lattice). Overall, this study further positions SECCM as an effective tool for analysing the structure-dependent corrosion-related behaviour of metal alloys at the nanoscale, particularly when combined with complementary structural characterisation (*e.g.*, EBSD and STEM) and computational analysis (*e.g.*, DFT calculations).

Acknowledgements

This work was supported by an iCASE award to L.Y. from the EPSRC and Tata Steel Research and Development. V.S. acknowledges financial support from the European Union's Horizon 2020 research and innovation programme under grant agreement 792948 (NELMA). C.L.B. acknowledges financial support from the Ramsay Memorial Fellowship Trust. P.R.U. gratefully acknowledges

support from a Royal Society Wolfson Research Merit Award and an EPSRC Programme Grant (EP/R018820/1). The authors also acknowledge Dr Digvijay Thakur from Tata Steel Research and Development for helpful discussions.

Appendix A. Supplementary data

Supplementary data to this article can be found online at https://doi.org/10.1016/j.electacta.2019.135267.

References

[1] R. Feser, Chapter 2.1 uniform corrosion of metals in acid, neutral and alkaline electrolytes, in: M. Stratmann, G. Frankel (Eds.), Corrosion and Oxide Films, Wiley-VCH, Germany, 2003, pp. 67–107.

[2] A. Schreiber, J.W. Schultze, M.M. Lohrengel, F. Kármán, E. Kálmán, Grain dependent electrochemical investigations on pure iron in acetate buffer pH 6.0, Electrochim. Acta 51 (2006) 2625–2630.

[3] A. Schreiber, C. Rosenkranz, M.M. Lohrengel, Grain-dependent anodic dissolution of iron, Electrochim. Acta 52 (2007) 7738–7745.

[4] M. Seo, M. Chiba, Nano-mechano-electrochemistry of passive metal surfaces, Electrochim. Acta 47 (2001) 319–325.

[5] M. Chiba, M. Seo, Mechanoelectrochemical properties of passive iron surfaces evaluated by an in situ nanoscratching test, J. Electrochem. Soc. 150 (2003). B525-B525.

[6] A. Shahryari, J.A. Szpunar, S. Omanovic, The influence of crystallographic orientation distribution on 316LVM stainless steel pitting behavior, Corros. Sci. 51 (2009) 677–682.

[7] H. Krawiec, Z. Szklarz, Combining the Electrochemical Microcell Technique and the Electron Backscatter Diffraction method to study the electrochemical behaviour of polycrystalline aluminium in sodium chloride solution, Electrochim. Acta 203 (2016) 426–438.

[8] K.A. Lill, A.W. Hassel, G. Frommeyer, M. Stratmann, Scanning droplet cell investigations on single grains of a FeAlCr light weight ferritic steel, Electrochim. Acta 51 (2005) 978–983.

[9] R. Oltra, Local electrochemical methods in corrosion research, in: R. Oltra, V. Maurice, R. Akid, P. Marcus (Eds.), Local Probe Techniques for Corrosion Research, CRC Press, USA, 2007, pp. 1–11.

[10] N.A. Payne, L. Stephens, J. Mauzeroll, The application of scanning electrochemical microscopy to corrosion research, Corrosion 73 (2017) 759–780.

[11] S. Amemiya, A.J. Bard, F.R.F. Fan, M.V. Mirkin, P.R. Unwin, Scanning electrochemical microscopy, Anal. Chem. 1 (2008) 95–131.

[12] M. Pahler, J.J. Santana, W. Schuhmann, R.M. Souto, Application of AC-SECM in corrosion science: local visualisation of inhibitor films on active metals for corrosion protection, Chemistry 17 (2011) 905–911.

[13] K. Eckhard, W. Schuhmann, Alternating current techniques in scanning electrochemical microscopy (AC-SECM), Analyst 133 (2008) 1486–1497.

[14] H. Böhni, T. Suter, A. Schreyer, Micro- and nanotechniques to study localized corrosion, Electrochim. Acta 40 (1995) 1361–1368.

[15] T. Suter, H. Böhni, A new microelectrochemical method to study pit initiation on stainless steels, Electrochim. Acta 42 (1997) 3275–3280.

[16] F. Andreatta, L. Fedrizzi, The use of the electrochemical micro-cell for the investigation of corrosion phenomena, Electrochim. Acta 203 (2016) 337–349.

[17] E.G. Webb, R.C. Alkire, Pit initiation at single sulfide inclusions in stainless steel, J. Electrochem. Soc. 149 (2002). B286-B286.

[18] F. Andreatta, M.M. Lohrengel, H. Terryn, J.H.W. De Wit, Electrochemical characterisation of aluminium AA7075-T6 and solution heat treated AA7075 using a micro-capillary cell, Electrochim. Acta 48 (2003) 3239–3247.

[19] N. Birbilis, R.G. Buchheit, Electrochemical characteristics of intermetallic phases in aluminum alloys, J. Electrochem. Soc. 152 (2005). B140-B140.

[20] N. Ebejer, A.G. Güell, S.C.S. Lai, K. McKelvey, M.E. Snowden, P.R. Unwin, Scanning electrochemical cell microscopy: a versatile technique for nanoscale electrochemistry and functional imaging, Annu. Rev. Anal. Chem. 6 (2013) 329–351.

[21] C.L. Bentley, M. Kang, P.R. Unwin, Scanning electrochemical cell microscopy: new perspectives on electrode processes in action, Curr Opin Electrochem 6 (2017) 23–30.

[22] C.L. Bentley, J. Edmondson, G.N. Meloni, D. Perry, V. Shkirskiy, P.R. Unwin, Nanoscale electrochemical mapping, Anal. Chem. 91 (2019) 84–108.

[23] C.L. Bentley, M. Kang, F. Maddar, F. Li, M. Walker, J. Zhang, P.R. Unwin, Electrochemical maps and movies of the hydrogen evolution reaction on natural crystals of molybdenite (MoS 2): basal vs, Edge Plane Activity, Chem Sci 8 (2017) 6583–6593.

[24] P.R. Unwin, A.G. Güell, G. Zhang, Nanoscale electrochemistry of sp^2 carbon materials: from graphite and graphene to carbon nanotubes, Acc. Chem. Res. 49 (2016) 2041–2048.

[25] B.D.B. Aaronson, C.H. Chen, H. Li, M.T.M. Koper, S.C.S. Lai, P.R. Unwin, Pseudo-single-crystal electrochemistry on polycrystalline electrodes: visualizing activity at grains and grain boundaries on platinum for the Fe^{2+}/Fe^{3+} redox reaction, J. Am. Chem. Soc. 135 (2013) 3873–3880.

[26] Y. Wang, E. Gordon, H. Ren, Mapping the nucleation of H2 bubbles on polycrystalline Pt via scanning electrochemical cell microscopy, J. Phys. Chem. Lett. 10 (2019) 3887–3892.

[27] R.G. Mariano, K. McKelvey, H.S. White, M.W. Kanan, Selective increase in CO_2 electroreduction activity at grain-boundary surface terminations, Science 358 (2017) 1187–1192.

[28] C.L. Bentley, C. Andronescu, M. Smialkowski, M. Kang, T. Tarnev, B. Marler, P.R. Unwin, U.P. Apfel, W. Schuhmann, Local Surface Structure and Composition Control the Hydrogen Evolution Reaction on Iron Nickel Sulfides, vol. 57, Angewandte Chemie - International Edition, 2018, pp. 4093–4097.

[29] C.L. Bentley, M. Kang, P.R. Unwin, Nanoscale structure dynamics within electrocatalytic materials, J. Am. Chem. Soc. 139 (2017) 16813–16821.

[30] C.L. Bentley, P.R. Unwin, Nanoscale electrochemical movies and synchronous topographical mapping of electrocatalytic materials, Faraday Discuss 210 (2018) 365–379.

[31] J.W. Hill, C.M. Hill, Directly mapping photoelectrochemical behavior within individual transition metal dichalcogenide nanosheets, Nano Lett. 19 (2019) 5710–5716.

[32] B. Tao, L.C. Yule, E. Daviddi, C.L. Bentley, P.R. Unwin, Correlative electrochemistry-microscopy of Li-ion (de)intercalation at series of individual LiMn2O4 particles, Angew. Chem. Int. Ed. 58 (2019) 4606–4611.

[33] L.C. Yule, C.L. Bentley, G. West, B.A. Shollock, P.R. Unwin, Scanning electrochemical cell microscopy: a versatile method for highly localised corrosion related measurements on metal surfaces, Electrochim. Acta 298 (2019) 80–88.

[34] R.C. Hudd, Sheet Steel: Low Carbon, Encyclopedia of Materials: Science and Technology2001, pp. 8456-8846.

[35] E.-S.M. Sherif, A.T. Abbas, H. Halfa, A.M. El-Shamy, Corrosion of high stength seel in concentrated sulfuric acid pickling solutions and its inhibition by 3-Amino-5-mercapto-1,2,3-triazole, Int JElectrochem Sci 10 (2015) 1777–1791.

[36] M.E. Snowden, A.G. Güell, S.C.S. Lai, K. McKelvey, N. Ebejer, M.A. O'Connell, A.W. Colburn, P.R. Unwin, Scanning electrochemical cell microscopy: theory and experiment for quantitative high resolution spatially-resolved voltammetry and simultaneous ion-conductance measurements, Anal. Chem. 84 (2012) 2483–2491.

[37] D. Momotenko, J.C. Byers, K. McKelvey, M. Kang, P.R. Unwin, High-speed electrochemical imaging, ACS Nano 9 (2015) 8942–8952.

[38] F. Hilbert, Y. Miyoshi, G. Eichkorn, W.J. Lorenz, Correlations between the kinetics of electrolytic dissolution and deposition of iron: I . The anodic dissolution of iron, J. Electrochem. Soc. 118 (1971) 1919–1926.

[39] I. Puigdomenech, Hydra and Medusa Software, KTH, Sweden.

[40] P. Giannozzi, S. Baroni, N. Bonini, M. Calandra, R. Car, C. Cavazzoni, D. Ceresoli, G.L. Chiarotti, M. Cococcioni, I. Dabo, A. Dal Corso, S. de Gironcoli, S. Fabris, G. Fratesi, R. Gebauer, U. Gerstmann, C. Gougoussis, A. Kokalj, M. Lazzeri, L. Martin-Samos, N. Marzari, F. Mauri, R. Mazzarello, S. Paolini, A. Pasquarello, L. Paulatto, C. Sbraccia, S. Scandolo, G. Sclauzero, A.P. Seitsonen, A. Smogunov, P. Umari, R.M. Wentzcovitch, Quantum espresso: a modular and open-source software project for quantum simulations of materials, J. Phys. Condens. Matter 21 (2009) 395502.

[41] W. Kohn, L.J. Sham, Self-consistent equations including exchange and correlation effects, Phys. Rev. 140 (1965) A1133–A1138.

[42] D. Vanderbilt, Soft self-consistent pseudopotentials in a generalized eigenvalue formalism, Phys. Rev. B 41 (1990) 7892–7895.

[43] A. Dal Corso, Pseudopotentials periodic table: from H to Pu, Comput. Mater. Sci. 95 (2014) 337–350.

[44] H.J. Monkhorst, J.D. Pack, Special points for Brillouin-zone integrations, Phys. Rev. B 13 (1976) 5188–5192.

[45] G.J. Martyna, M.E. Tuckerman, A consistent and accurate ab initio parametrization of density functional dispersion correction (DFT-D) for the 94 elements H-Pu, J. Chem. Phys. 132 (2010) 154104.

[46] O. Andreussi, I. Dabo, N. Marzari, Revised self-consistent continuum solvation in electronic-structure calculations, J. Chem. Phys. 136 (2012), 064102.

[47] P. Giannozzi, O. Andreussi, T. Brumme, O. Bunau, M. Buongiorno Nardelli, M. Calandra, R. Car, C. Cavazzoni, D. Ceresoli, M. Cococcioni, N. Colonna, I. Carnimeo, A. Dal Corso, S. de Gironcoli, P. Delugas, R.A. DiStasio, A. Ferretti, A. Floris, G. Fratesi, G. Fugallo, R. Gebauer, U. Gerstmann, F. Giustino, T. Gorni, J. Jia, M. Kawamura, H.Y. Ko, A. Kokalj, E. Küçükbenli, M. Lazzeri, M. Marsili, N. Marzari, F. Mauri, N.L. Nguyen, H.V. Nguyen, A. Otero-de-la-Roza, L. Paulatto, S. Poncé, D. Rocca, R. Sabatini, B. Santra, M. Schlipf, A.P. Seitsonen, A. Smogunov, I. Timrov, T. Thonhauser, P. Umari, N. Vast, X. Wu, S. Baroni, Advanced capabilities for materials modelling with Quantum ESPRESSO, J. Phys. Condens. Matter 29 (2017).

[48] D. Vanderbilt, S.G. Louie, Total energies of diamond (111) surface reconstructions by a linear combination of atomic orbitals method, Phys. Rev. B 30 (1984) 6118–6130.

[49] F. Trani, D. Ninno, G. Cantele, G. Iadonisi, K. Hameeuw, E. Degoli, S. Ossicini, Screening in semiconductor nanocrystals:Ab initioresults and Thomas-Fermi theory, Phys. Rev. B 73 (2006).

[50] S.R. Billeter, A.J. Turner, W. Thiel, Linear scaling geometry optimisation and transition state search in hybrid delocalised internal coordinates, Phys. Chem. Chem. Phys. 2 (2000) 2177–2186.

[51] C.G. Williams, M.A. Edwards, A.L. Colley, J.V. Macpherson, P.R. Unwin, Scanning micropipet contact method for high-resolution imaging of electrode surface redox activity, Anal. Chem. 81 (2009) 2486–2495.

[52] M. Pourbaix, Atlas of Electrochemical Equilibria in Aqueous Solutions. IV.

Establishment and Interpretation of Potential-pH Equilibrium Diagrams, first ed., Pergamon Press, London, 1966.
[53] E. McCafferty, Introduction to Corrosion Science, Springer, London, 2010.
[54] L.C. Yule, V. Shkirskiy, J. Aarons, G. West, C.L. Bentley, B.A. Shollock, P.R. Unwin, Nanoscale Active sites for the hydrogen evolution reaction on low carbon steel, J. Phys. Chem. C 123 (2019) 24146–24155.
[55] A.J. Davenport, L.J. Oblonsky, M.P. Ryan, M.F. Toney, The structure of the passive film that forms on iron in aqueous environments, J. Electrochem. Soc. 147 (2000) 2162–2173.
[56] K. Fushimi, K. Miyamoto, H. Konno, Anisotropic corrosion of iron in pH 1 sulphuric acid, Electrochim. Acta 55 (2010) 7322–7327.
[57] M. Liu, D. Qiu, M.-C. Zhao, G. Song, A. Atrens, The effect of crystallographic orientation on the active corrosion of pure magnesium, Scr. Mater. 58 (2008) 421–424.
[58] A.C. Lasaga, A. Lüttge, A model for crystal dissolution, Eur. J. Mineral. 15 (2003) 603–615.
[59] P.R. Unwin, J.V. Macpherson, New strategies for probing crystal dissolution kinetics at the microscopic level, Chem. Soc. Rev. 24 (1995) 109–119.
[60] D.A. Sverjensky, Linear free energy relations for predicting dissolution rates of solids, Nature 358 (1992) 310–313.
[61] U. Angst, B. Elsener, C.K. Larsen, Ø. Vennesland, Chloride induced reinforcement corrosion: rate limiting step of early pitting corrosion, Electrochim. Acta 56 (2011) 5877–5889.